Towards understanding stochastic fracture performance of cement paste at micro length scale based on numerical simulation

Zhang, Hongzhi; Šavija, Branko; Schlangen, Erik

DOI
10.1016/j.conbuildmat.2018.06.167

Publication date
2018

Document Version
Final published version

Published in
Construction and Building Materials

Citation (APA)
Zhang, H., Šavija, B., & Schlangen, E. (2018). Towards understanding stochastic fracture performance of cement paste at micro length scale based on numerical simulation. *Construction and Building Materials*, *183*, 189-201. https://doi.org/10.1016/j.conbuildmat.2018.06.167

Construction and Building Materials 183 (2018) 189–201

Contents lists available at ScienceDirect

Construction and Building Materials

journal homepage: www.elsevier.com/locate/conbuildmat

Towards understanding stochastic fracture performance of cement paste at micro length scale based on numerical simulation

Hongzhi Zhang *, Branko Šavija, Erik Schlangen

Microlab, Faculty of Civil Engineering and Geosciences, Delft University of Technology, 2628 CN Delft, The Netherlands

HIGHLIGHTS

- The stochastic micromechanical properties of cement paste were predicted.
- Results show good agreement with data in the literature.
- Specimen with lower w/c ratio has higher and less variable strength and elasticity.
- A strong size effect exists in the modulus/stress ratio of cement paste.

ARTICLE INFO

Article history:
Received 14 January 2018
Received in revised form 7 April 2018
Accepted 19 June 2018

Keywords:
X-ray computed tomography
Cement paste
Micromechanics
Lattice modelling

ABSTRACT

This work presents a study of stochastic fracture properties of cement paste at the micro length scale based on a combination of X-ray computed tomography (XCT) technique and discrete lattice type fracture model. Thirty virtual specimens consisting of pore, outer hydration products, inner hydration products and anhydrous cement particles were extracted from 3D images obtained through XCT from real cement paste samples. These virtual specimens were subjected to a computational uniaxial tension test to calculate their tensile strengths and elastic moduli. The predicted stochastic strengths were analysed using Weibull statistics, showing that specimens with lower w/c ratio yield higher strength and less variability. The strength-porosity and modulus-porosity relations were investigated based on existing empirical models. It was shown that existing models can predict the properties in the studied porosity range quite accurately, with the exponential model having the highest determination coefficient among all the models for both relations. Finally, by comparing the existing data in the literate, it is found that the smaller cement paste specimens have higher modulus/tensile strength ratio, which indicates that they are able to have more strain at the peak load.

1. Introduction

Cement paste is a porous and heterogeneous material [1]. As a basic binding material in concrete, it has generated considerable research interest. It is generally accepted that fracture of conventional concrete starts from micro-cracks in the cement paste where local tensile stress exceeds its tensile strength. Understanding the deformation and fracture performance (i.e. tensile strength and elastic modulus) of cement paste at the micro-scale is therefore of significant practical importance and scientific interest.

Nanoindentation has been utilized for quantification of local properties such as elasticity and hardness of micro level components in the matrix [2–6] for a long time. Based on the same principles, peak-force tapping atomic force microscopy (AFM) can be applied as an alternative tool to quantify the local elastic properties [7]. These techniques provide a meaningful experimental input for analytical and numerical models used to calculate the global micromechanical properties of cement paste [8–13] which can be further used as input within a multi-scale framework to simulate the macroscopic mechanical performance of concrete [14–16].

Although a lot of valuable micromechanical information was obtained to set a basis for understanding and improving the macroscopic mechanical performances, stochastic micromechanical properties of cement paste have been rarely studied due to the complex and time-consuming modelling procedure. Furthermore, for a number of reasons that include problems with producing and measuring miniaturized mechanical samples, the predicted mechanical properties are difficult to verify experimentally at the micro scale. As reported in [17,18], a pioneering work on experimental micromechanics of cement paste has been conducted at the Delft University of Technology. Micrometre scale specimens

* Corresponding author.
E-mail address: h.zhang-5@tudelft.nl (H. Zhang).

https://doi.org/10.1016/j.conbuildmat.2018.06.167
0950-0618/

with a cubic dimension of 100 μm were produced by a micro dicing saw and ruptured by a diamond wedge tip mounted on a nano-indentation system. The splitting tensile strength of the tested specimens was derived from the recorded critical load and the test results show a large dispersion, as expected for a highly heterogeneous material at this scale. For a specific ruptured specimen, detailed microstructure information cannot be obtained due to technical and instrumental limitations. Therefore, it is hard to correlate the fracture properties with its microstructure for quantitative assessment at the micro scale. Instead, application of a microstructure-informed numerical model [12,13,19,20] offers an opportunity to achieve this. Such a model requires a detailed microstructure and micromechanical properties of individual components in the material. The 3D microstructure can be obtained either by modelling or experiments. Although numerical cement hydration models have clear advantages in terms of time effort and ease of obtaining, cement particles are commonly modelled as spherical in such models [21,22]. This has an influence on the simulated hydration of cement [23]. Furthermore, it is reported that the assumed morphology of hydrates in the simulated microstructure significantly influences micromechanics-based elastic stiffness estimates of cement paste, particularly at very early age [24]. Furthermore, it is worth mentioning that a popular digital microstructural model CemHyd3D [25] permits a direct representation of multiphase, multi-size and non-spherical cement particles using SEM images. However, it is reported by Hain and Wriggers [26] that, because of random based rules, the parts of microstructure in CemHyd3D are distributed very evenly. In particular, there are no accumulations of pores in its simulated microstructure as observed in X-ray computed tomography (XCT), which is now becoming a widely used technique for three-dimensional microstructure characterisation of cement-based materials [27–29]. The basic idea of XCT is simple [30]: rotate a material under X-ray scanning and collect the absorbed X-ray on a detector to create a series 2D projections from which the density spatial distribution of phases inside the material can be visualised by greyscale levels. In terms of cement paste, pores have the lowest greyscale level, while anhydrous cement grains have the highest greyscale level. Based on the histogram of greyscale levels, image segmentation can be conducted to isolate different components, namely pore, inner and outer hydration products, and anhydrous cement grains. Note that, as reported in [31], C–S–H and nano-CH are associated, not merely as a simple biphase mixture. For simplification, the inner and outer hydration products in the current study are referred to inner (high density) and outer (low density) C-S-H gel, respectively. In order to show the stochastic mechanical properties of cement paste at micro-scale, for each w/c ratio (0.3, 0.4 and 0.5), ten microstructures with a cubic dimension of 100 μm^3 were sliced from XCT images of cement paste specimens cured for 28-days. These microstructures were then used as input for fracture simulations performed using a lattice type fracture model. The computational uniaxial tension test was performed on three different loading directions for each cubic specimen, making it 30 simulations for each w/c.

Lattice type fracture model is one of the most popular microstructure informed numerical models to study fracture process and stress-strain response of cement-based materials. Its main strength is the simulated detailed crack patterns which resemble experimental observations very closely [32–35]. As an experimental procedure at the micro scale has been designed and utilized to calibrate the input parameters in this model recently, the predicted micromechanical properties of cement paste are expected to be more reliable [13] compared to previous research. Therefore, lattice fracture model is adopted in this work to simulate the fracture behaviour of cement paste based on XCT obtained microstructure. For better understanding of its stochastic fracture performance, a Weibull statistical analysis is conducted to analyse the simulation results. In addition, several widely used empirical equations describing the effects of porosity on mechanical properties for cement-based materials were examined and extended to the cement paste at micro-scale on the basis of the simulated results.

2. Virtual specimen generation

2.1. X-ray CT scanning

In the experimental program, small cement paste prisms with cubic cross-section of 400 μm × 400 μm and length of 1 mm were produced and scanned by a microcomputed tomography system. Cement pastes were prepared with standard grade CEMI 42.5 N Portland cement and deionized water. The w/c ratios of used paste were 0.3, 0.4 and 0.5.

The cement and deionized water were carefully mixed with the designed w/c ratio, vibrated and poured into a PVC cylinder (diameter, 24 mm, height 39 mm). To prevent bleeding, the cylinder was rotated with a speed of 2.5 revolutions per minute for 24 h. The specimens were sealed in the cylinder and stored in a room with temperature of 20 °C. After sealed curing for 28 days, the specimens were demoulded and a slice with a thickness of 2 mm in the middle part was cut out using a precision diamond saw. The slice was then attached on the glass substrate using a UV bonding resin and grinded down to 400 μm by diamond ring grinding discs with grit size of 125 μm and 30 μm in descending order. To ensure that both surfaces of the slice are smooth, the slice was detached when reaching 1 mm thickness, flipped over and reattached on the glass substrate. The same grinding procedure was performed on the new surface. A micro dicing saw was then used to cut through the slice to produce small prisms with a square cross section of 400 × 400 μm^2 as presented in Fig. 1a. The back-scattered electron (BSE) image of the small prism is shown in Fig. 1b.

The small prism was clamped by a special holder (Fig. 2) and fixed in the rotatable stage of a high resolution XCT scanner (Phoenix Nanotom, Boston, MA, USA) for acquiring raw greyscale images with a source voltage of 120 kv and current of 60 μA. The sample was rotated 360° and, in total, 2880 shadow projections with a pixel size of 0.5 μm were acquired on the digital GE DXR detector (3072 × 2400 pixels). Each projection image was averaged with an exposure time of 6 s. The reconstruction work was conducted by the Phoenix Datos|x software. To reduce the influence of beam hardening in the XCT experiment, a cuboid region of interest (ROI) with a cross-section of 200 μm × 200 μm and length of 500 μm was extracted from the middle region of the specimen for the analysis (Fig. 2b). The mesh discretization in the fracture model is correlated with the voxel size from the material structure, and in total 90 computational uniaxial tensile tests were to be performed, which means a huge computational effort were needed for this study. For this reason, the resolution was reduced to 2 μm^3/voxel through a "median method" implemented in the X-ray reconstruction software. Finally, a 3D stack of 8-bit cross-section images were generated.

2.2. Microstructure characterisation

Quite a few image segmentation methods have been suggested in the literature. Herein, a global thresholding method is applied [29,36,37]. As shown in Fig. 3, based on the greyscale-level histogram, four threshold greyscale levels were defined to segment pores, anhydrous cement grains, inner hydration products and outer hydration products from the raw grey images. The reader is referred to [13] for further information on the image segmentation, only a short description is addressed herein: (1) T_1, the

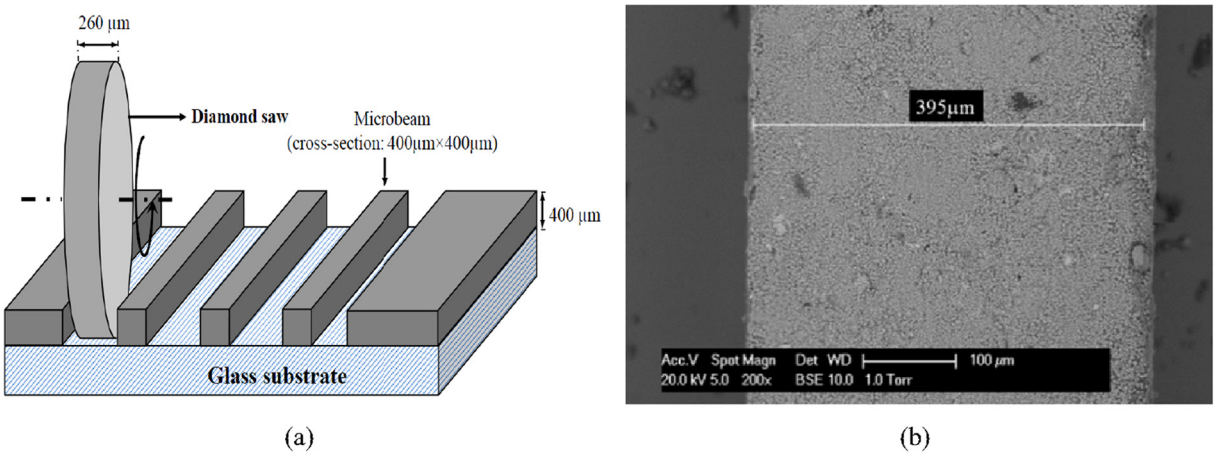

Fig. 1. Schematic view of small prisms preparation. (a) cutting small prisms from thin slice. (b) BSE image of a small prism with measurements.

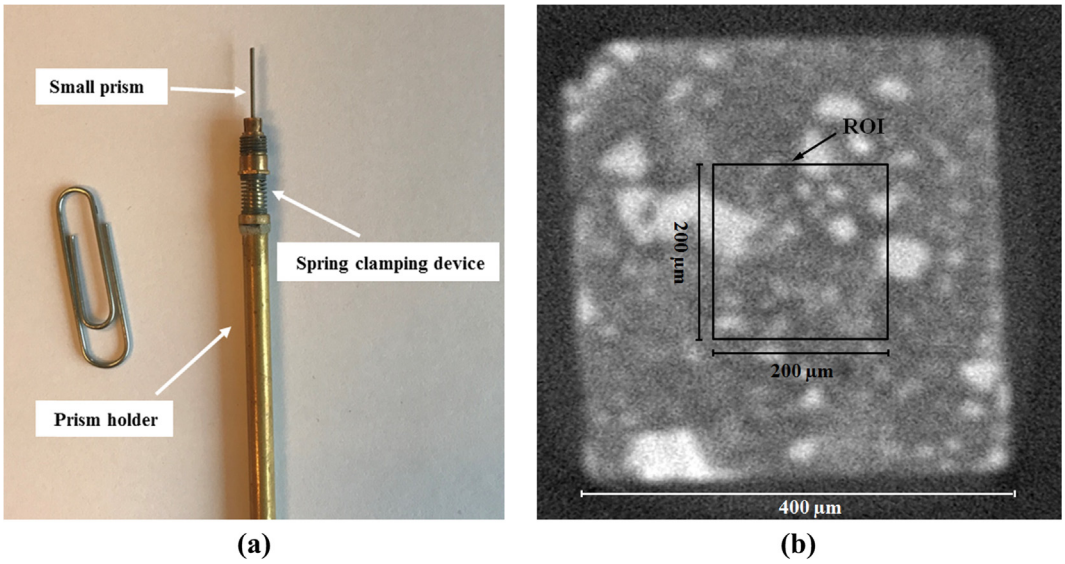

Fig. 2. (a) Small prism clamped on the special holder for CT scanning, after [20]; (b) an example cross sectional XCT image of ROI.

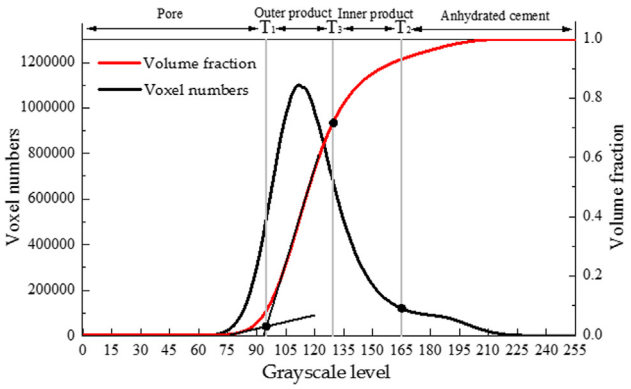

Fig. 3. Image segmentation through greyscale level histogram of CT images.

inflection of the cumulative curve was considered as the upper threshold value for pores; (2) T_2, the greyscale value corresponding to a transition point, at which a change of the tangent slope occurs, was used as the lower threshold level for anhydrous particle, and hydration degree can be estimated according to [38]; (3) T_3, the threshold level for inner/outer hydration products was selected as the one satisfying the theoretical amount according to an analytical equation proposed by Tennis and Jennings [6] in which hydration degree and w/c ratio are used as input. The hydration degree α was estimated using the following equation:

$$\alpha = \frac{\frac{V_h}{\upsilon}}{\frac{V_h}{\upsilon} + V_a} \quad (1)$$

where V_h and V_a denote volume fractions of hydration products and anhydrous cement grains segmented from step 2, respectively; υ is the volume reaction product/volume reactant ratio and assumed as 2.2 [38]. As a result, raw greyscale images were converted to quaternary images. Cubic specimens with a dimension of 100 μm × 100 μm × 100 μm (50 × 50 × 50 voxels) were randomly extracted from the segmented images as shown in Fig. 4 for micromechanical properties evaluation.

For each w/c ratio (i.e. 0.3, 0.4 and 0.5), one prism was scanned, and 10 virtual specimens were extracted from each prism. Based on the described procedure, the segmented volume fraction of pore, anhydrous cement grains and hydration degree of each scanned prism are listed in Table 1. The hydration degree is quite close to the one reported by Haecker et al. [39] using non-evaporable water content method (for w/c = 0.3: 63.0%, w/c = 0.4: 80.6% and w/c = 0.5: 88.4%). One should keep in mind that, owing

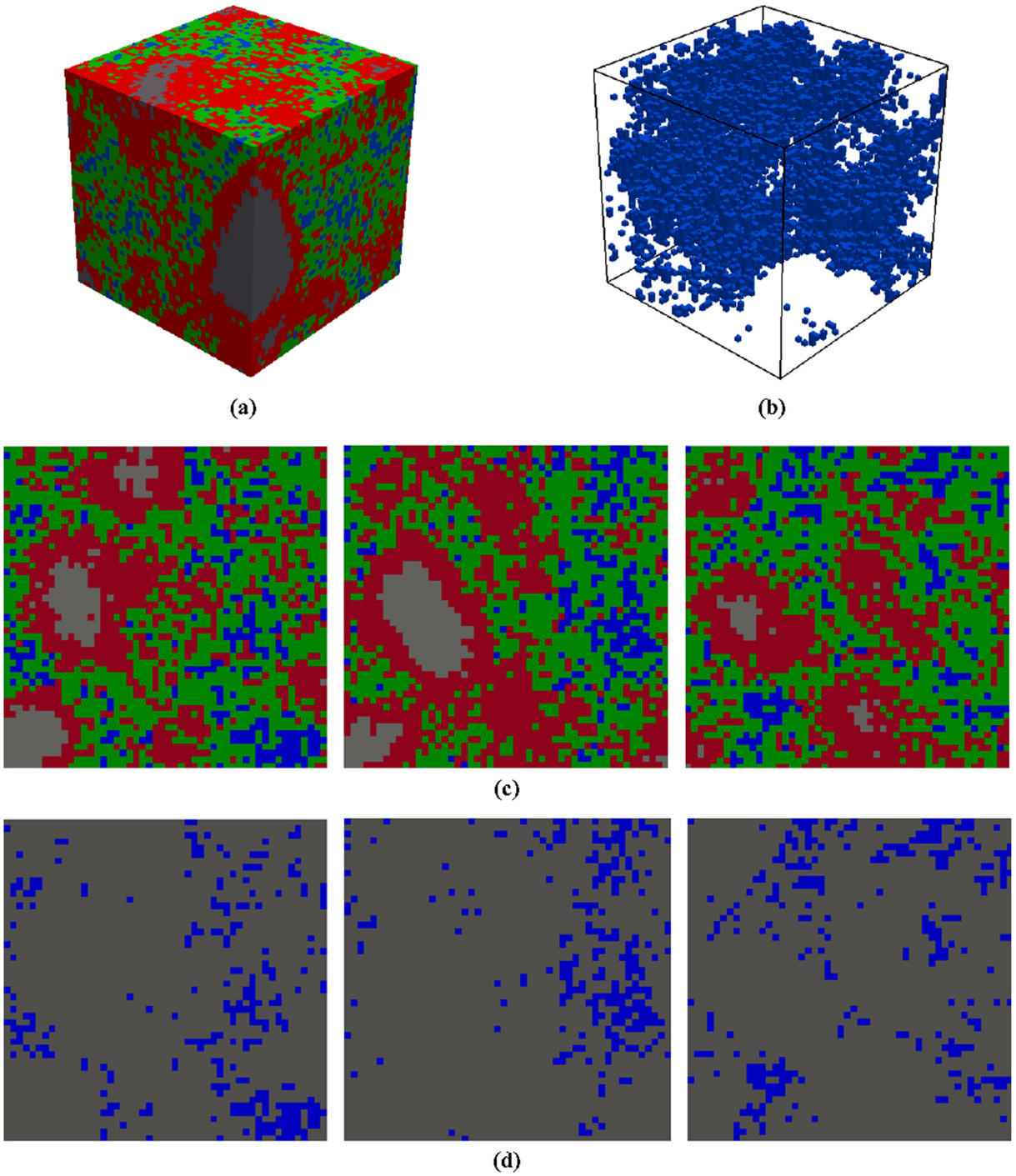

Fig. 4. Example of a virtual specimen (100 μm × 100 μm × 100 μm, 50 × 50 × 50 voxels) with w/c ratio of 0.4: (a) spatial distribution of all phases; (b) spatial distribution of pore phase; slices of the specimen at 1/4, 1/2 and 3/4 height from left to the right of (c) all phases distribution and (d) the pore phase distribution (green – outer product; red – inner product; grey – anhydrous grains, blue – pore). (For interpretation of the references to colour in this figure legend, the reader is referred to the web version of this article.)

Table 1
Details of segmented microstructures.

w/c	Porosity (%)	Anhydrous cement grains (%)	Hydration degree (%)
0.3	8.44	15.30	69.65
0.4	11.84	10.64	74.99
0.5	17.50	8.02	80.85

to the limitation of image resolution, pores smaller than 2 μm are not detectable and are mixed within the segmented solid phases [40–42]. Therefore, the total porosity derived from CT images is significantly lower than the theoretical total porosity predicted by Powers model (for w/c = 0.3: 17.80%, w/c = 0.4: 23.3% and w/c = 0.5: 29.2%) [43] and mercury intrusion porosimetry (MIP) test performed on similar pastes (for w/c = 0.3: 17%, w/c = 0.4: w/c = 23%

and 0.5: 31%) [44] which include the capillary pores smaller than 2 μm as well as part of gel pores.

3. Modelling

In the lattice fracture model [33,45], a material volume is represented by a network of beam elements having linear elastic behaviour. A Timoshenko beam element is commonly used to take shear deformation into account considering the low ratio of length and height of beam elements in the network [46]. A set of linear elastic analyses is then performed by calculating the stress distribution at each element for an imposed particular external boundary condition. Normal force and bending moments in lattice beam elements are both taken into account by the following general relation:

$$\sigma = \alpha_N \frac{N}{A} + \alpha_M \frac{\max(M_x, M_y)}{W} \quad (2)$$

where A denotes the beam cross-sectional area, W is the cross-sectional moment of resistance; N is the normal force along the element. M_x and M_y are the local bending movements in the local coordinate system. α_N and α_M represent the normal force influence factor and the bending influence factor. Their values are commonly adopted as 1.0 and 0.05, respectively [47]. These values were also adopted herein. The influence of different values of these parameters on the concrete fracture response is discussed elsewhere [48]. Torsion is not included in the fracture law in the current study for simplicity. In every analysis step, loading is increased until exactly one beam in the mesh has a stress/strength ratio equal to one. This beam is then removed from the mesh. The mesh is then updated and relaxed. This loading procedure is repeated until a predefined stopping criterion (e.g. load or displacement). Consequently, the fracture pattern of the investigated material volume at each step can be obtained as well as their load-displacement response (grey line in Fig. 5). The zig-zag observed in the response can be explained by the fact that after a beam element is removed, much less load is needed to break the next beam, after which again an increasing load is required to continue further [49] and shows that local instabilities occurs during crack formation and propagation [47]. A smoothening technique as shown in the sketch (Fig. 5) is usually applied to overcome this zig-zag for comparison with the load-displacement curves recorded in the laboratory during experiments.

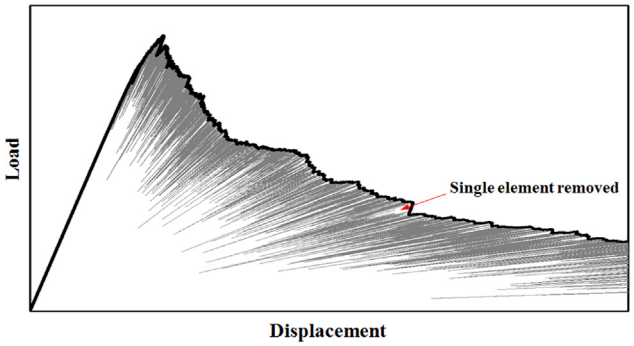

Fig. 5. A sketch of the smoothening of load-displacement obtained from a lattice simulation.

This model can be used to study the progressive damage of a disordered system [50]. This is achieved by assigning local mechanical properties randomly according to various probability distributions [51] or accordingly on the basis of a specific material structure [20]. Herein the digital material structure is used. The procedure to generate the network and assign locally brittle behaviour is as follows:

A cubic domain with the same dimension of the investigated microstructure is divided into a cubic grid with a cell size of 2 μm^3 (same dimension to the voxel size of virtual specimens). Then, a sub-cell is defined within each cell. The nodes are then randomly positioned in these sub-cells. A parameter is defined as the ratio between length of sub-cell and cell to represent the randomness of the mesh. In order to avoid big variations in length of elements and introduce geometry disorder of material texture, a randomness of 0.5 is adopted.

Delaunay triangulation is then performed on a set of nodes as described by [52], see Fig. 6a. A discrete lattice mesh having 125,000 nodes and 937,247 elements is constructed. The mesh configuration that is chosen results in a Poisson's ratio of about 0.18 for the global performance.

A microstructure overlay procedure is conducted to determine the beam element type according to the locations of its end nodes, as shown in Fig. 6b. Elastic modulus of a beam element is ascribed with the harmonic average of the two connected phases, while the tensile strength is assigned as the lower value of the two [15,53]. The nodes within the pore voxels and the elements connecting to them are removed from the mesh as the initial defects in the system. The mechanical parameters of each single phase used in this study are presented in Table 2. It is important to notice that these hydration products are averages overall all types of hydrates

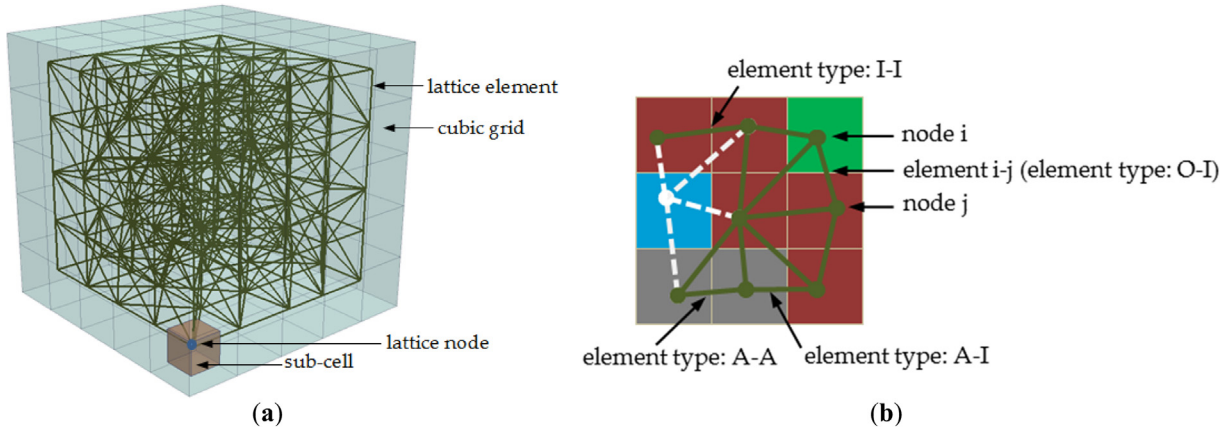

Fig. 6. Schematic view of lattice model generation: (a) lattice network construction (5 × 5 × 5); (b) microstructure overlay procedure for 2D lattice mesh (green – outer product; red – inner product; grey – anhydrous cement, blue – pore). (For interpretation of the references to colour in this figure legend, the reader is referred to the web version of this article.)

Table 2
Assigned local mechanical properties of individual phases at micro scale [13].

Phase	Young's modulus (GPa)	Strength (MPa)
Anhydrous cement	99	683
Inner product	31	92
Outer product	25	58

(including Portlandite, Ettringite, and Calcium Silicate Hydrates (C–S–H) of different mass densities) and small capillary pores. As the main purpose of this work to investigate the stochastic micromechanical behaviour of cement paste, for the sake of simplification, deterministic values of micromechanical parameters were used as input. Elastic moduli are assumed to be equal to the nanoindentation measurements for individual phases [9]. The tensile strengths are taken from a previous study by the authors [13], wherein a micro scale experiment is developed to calibrate these values. Briefly, a Berkovich tip mounted on a nanoindentation system was used to rupture a micro cement paste cube (100 μm × 100 μm × 100 μm). The fracture behaviour of the cube is then simulated by lattice fracture model with the same discretization as the one used in the current work. The tensile strengths of local phases were assumed to be proportional to their hardness and were optimized until the predicted load-displacement curve and fracture pattern were comparable to the experimental observations. It is emphasized that the local micromechanical properties should be the representative of the XCT resolution. This is because, with resolution variation, different amounts of capillary porosity or defects may be included in the segmented hydration products thereby introducing different micromechanical properties of the voxel. Note that similar values to those obtained by the authors in previous studies were obtained by Hlobil et al. [14] through an inverse analysis at a higher scale. With these assumptions, six types of elements are generated, as listed in Table 3.

The computational uniaxial tensile test was performed by applying a nodal displacement at one side and fixing the deformation of nodes at the opposite side, as shown in Fig. 7. Considering the heterogeneity of this material, fracture behaviour along all three directions of each specimen was investigated.

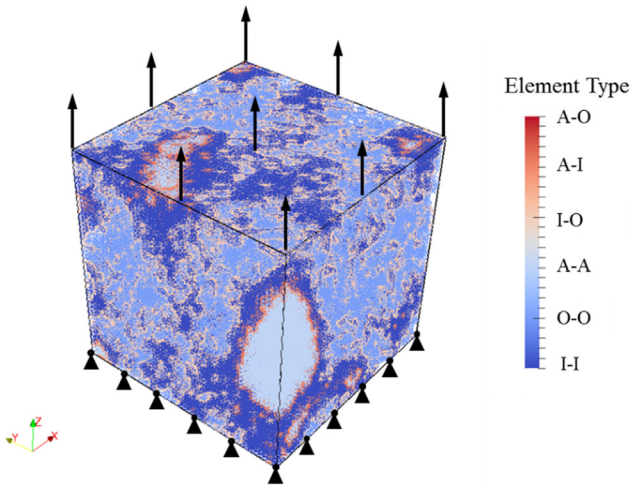

Fig. 7. Computational uniaxial tensile test of S1 at Z direction.

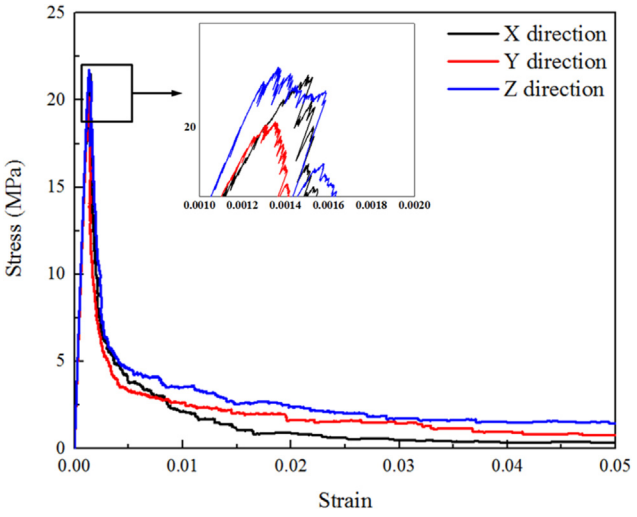

Fig. 8. Comparison of simulated stress strain curves of one specimen with w/c ratio of 0.4 under uniaxial tension from three directions.

4. Results and discussion

4.1. Modelling results

As an example, the simulated stress-strain diagrams of uniaxial tension tests of a specimen tested in different directions are shown in Fig. 8. The Young's modulus E can be computed from the initial slope of the curve, while tensile strength σ_f corresponds to the peak point. Fracture energy G_f is calculated from the post-peak part of the stress-strain curve as:

$$G_f = \int_{u1}^{u2} \sigma du \tag{3}$$

where σ is the stress and u the displacement; u_1 corresponds to the displacement at peak stress; u_2 denotes displacement at failure state and is regarded as 5 μm in this study. Note that the calculated fracture energy would be somewhat different if a different "cut-off" displacement was selected, but the main purpose of this work was to compare the fracture energy between different specimens. Results of all 90 simulations are listed in Table 4. Clearly, the strengths obtained at the microscale are relatively high compared with conventional laboratory centimetre sized samples (3–6 MPa) [54]. A similar trend was observed in other quasi-brittle materials such as nuclear graphite both experimentally [55] and numerically [56]. This is attributed to the fact that at micro-scale, samples are free from air voids or defects larger than the sample size. However, a large scatter is present in the simulated data as a result of the small volume of material sampled. The average results of each w/c

Table 3
Lattice element types and their mechanical properties [13].

Element type	Phase 1	Phase 2	Young's modulus (GPa)	Strength (MPa)
A-A	Anhydrous cement	Anhydrous cement	99	683
I-I	Inner product	Inner product	31	92
O-O	Outer product	Outer product	25	58
A-I	Anhydrous cement	Inner product	47	92
I-O	Inner product	Outer product	28	58
A-O	Anhydrous cement	Outer product	40	58

Table 4
Outcome of computational uniaxial tension tests.

w/c ratio	Sample	Porosity (%)	Tensile strength (MPa)			Young's modulus (GPa)			Fracture energy (J/m^2)		
			X	Y	Z	X	Y	Z	X	Y	Z
0.3	S1	7.00	28.19	27.07	27.68	28.51	28.15	28.14	9.02	9.45	6.16
	S2	6.26	30.19	25.67	27.69	28.90	28.37	28.77	7.70	7.20	11.50
	S3	4.77	31.50	29.30	29.73	32.13	31.63	30.34	8.10	15.41	11.20
	S4	6.95	26.53	25.55	25.54	28.42	28.22	28.45	13.08	11.68	9.88
	S5	6.86	26.99	22.68	26.11	26.11	26.63	27.05	9.01	8.66	9.61
	S6	6.99	22.43	25.34	26.70	26.70	25.11	25.42	13.88	9.96	7.52
	S7	12.56	20.80	21.21	18.43	23.10	22.49	22.17	10.49	9.40	7.77
	S8	8.54	23.89	24.38	19.60	31.43	28.33	26.46	8.77	9.49	7.52
	S9	5.10	32.13	28.07	24.16	33.69	32.34	30.34	13.25	10.09	14.51
	S10	9.79	26.40	24.67	24.65	25.07	24.67	24.82	9.87	9.41	8.67
0.4	S1	11.04	21.50	20.15	21.73	21.73	21.44	21.25	6.11	8.75	12.46
	S2	15.86	17.85	15.91	16.40	21.75	18.12	17.72	7.22	7.87	8.94
	S3	11.92	18.91	17.45	20.20	23.36	22.92	23.12	10.99	9.48	6.72
	S4	11.07	21.33	19.90	21.20	21.20	22.86	22.54	8.25	12.60	9.71
	S5	17.18	15.67	15.96	13.93	19.30	19.25	18.48	5.57	5.89	5.82
	S6	11.53	19.98	15.76	22.60	22.60	20.64	19.86	8.76	8.78	7.69
	S7	11.35	20.57	20.88	18.92	24.98	25.31	22.42	8.26	11.54	7.83
	S8	13.50	17.65	18.01	16.53	21.83	19.08	19.20	9.69	6.08	6.26
	S9	9.76	24.40	20.02	21.66	21.66	22.61	22.52	10.63	9.83	5.33
	S10	18.82	16.44	17.69	9.76	19.31	19.19	15.80	4.93	5.89	4.17
0.5	S1	18.85	15.13	15.18	10.50	17.13	16.88	15.23	5.70	4.47	5.28
	S2	12.32	21.73	20.15	20.98	21.24	20.84	21.02	6.29	6.80	5.83
	S3	25.01	8.71	10.21	8.49	13.09	12.61	11.20	3.54	4.57	3.73
	S4	14.76	16.86	19.03	16.31	19.43	21.42	17.06	6.20	5.96	7.05
	S5	23.88	13.66	9.55	8.76	15.49	13.10	12.57	8.64	3.41	4.26
	S6	20.85	12.44	13.07	9.47	15.51	15.28	13.13	2.96	4.42	4.90
	S7	7.77	20.08	25.62	20.21	27.44	29.49	25.95	7.16	4.98	5.96
	S8	12.68	18.14	20.43	14.49	20.08	22.18	19.61	5.94	7.30	5.80
	S9	11.29	20.15	20.06	17.26	23.67	24.61	21.86	8.90	8.90	7.43
	S10	9.55	22.00	23.19	15.63	24.93	26.33	22.45	5.78	7.64	6.16

ratio are summarized in Table 5. Although 10 specimens covering 10^5 μm^3 were extracted from the segmented images for each w/c ratio, still a bit difference of the averaged volume fraction of porosity and anhydrous cement particle were found between the investigated 10 specimens and the scanned prism (Table 1). Recently, such high tensile strengths were experimentally observed by rupturing the same size specimens through a nanoindentation system [18]. Furthermore, even higher strength is expected for samples at smaller length scale (few microns) [57], where distinct cement hydration phases like inner and outer hydration products containing capillary and gel pores can be sampled as micro cantilever beams. The final fracture pattern of one of the specimens is presented in Fig. 9. More than one main crack is observed in the final failure mode, which was attributed to the distributed pores which act as initial defects and anhydrous cement grains existing as "stiff inclusions" in the material and thereby deflecting the cracks. As the crack patterns are not identical, the strength property varies more than Young's modulus which is mostly influenced by the components and their relative amounts. Fig. 10 shows the fracture propagation of the presented specimen under Z direction loading. As can be seen, micro-cracks initiate around the middle part of the specimen and spread further until the final failure. In addition, an outline of an anhydrous cement grain is clearly observed in Fig. 10c, similar to the observation in conventional concrete, in which the micro-cracks always outline the aggregates [58,59]. In addition, as expected, the predicted mechanical properties decrease and become more variable with increasing w/c ratio. As presented in Fig. 11, the predicted average Young's moduli of cement pastes with different w/c ratios almost coincide with the experimental values from elastic resonance measurements [39] and show a good agreement with those from other micromechanical models [2,11,12,16,60]. The only exception is the predicted modulus of cement paste with w/c ratio 0.3 from [11], which is higher compared with the result in this work, but similar to the result of S9 at X direction (33.69 GPa, see Table 4). Therefore, the difference between the predicted modulus in the literature can be attributed the stochastic nature of this material. One should note that, to make the data from literature comparable to the current work, the corresponding hydration degree was used to extract results from references [11,16,60]. A Poisson's ratio of 0.24 (same as assumed in [60]) was used to convert bulk modulus from their work to Young's modulus.

4.2. Weibull analysis of strength

Weibull analysis has been widely used for characterising the scatter in measured fracture strength (which is mostly governed by the weakest link in the system) of a group of specimens that

Table 5
Summary of simulated micromechanical properties.

w/c ratio	Porosity (%)	Anhydrous cement grains (%)	Tensile strength (MPa)	Young's modulus (GPa)	Fracture energy (J/ m^2)
0.3	7.48 ± 2.18	14.70 ± 2.86	25.78 ± 3.29	27.73 ± 2.91	9.94 ± 1.50
0.4	13.20 ± 2.89	9.91 ± 2.44	18.63 ± 2.99	21.067 ± 3.01	8.07 ± 1.62
0.5	15.70 ± 5.76	7.24 ± 1.42	15.97 ± 5.02	19.36 ± 5.03	5.86 ± 1.30

Note: the data in table is addressed as: average ± standard deviation (variation coefficient).

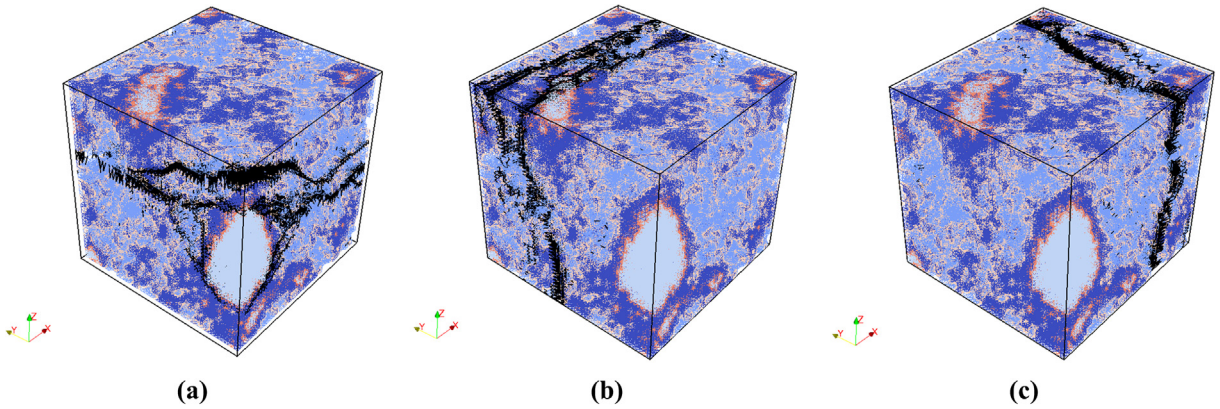

Fig. 9. One cracked and deformed specimen with w/c ratio of 0.4 under uniaxial tension in three directions: (a) Z (b) Y and (c) X at failure stage (black-cracked element; Deformations have been scaled for clarity).

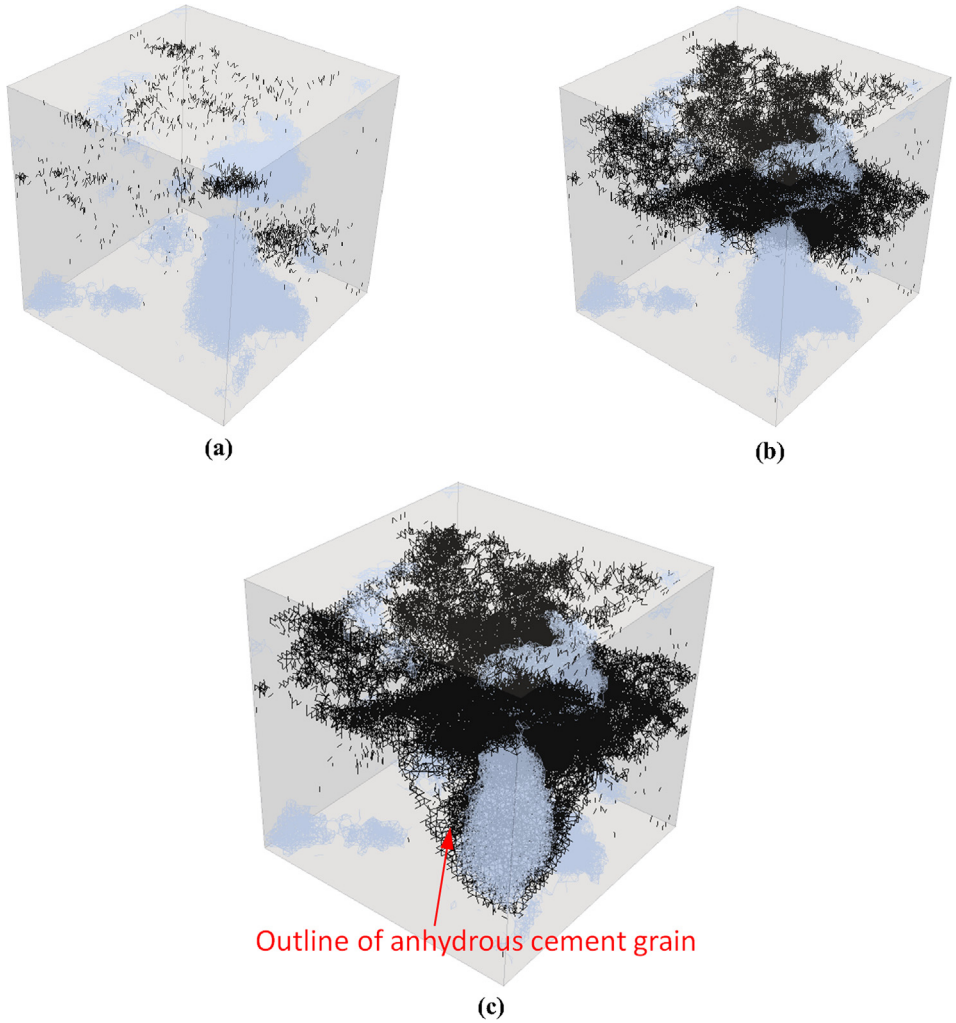

Fig. 10. Fracture pattern of one specimen with w/c ratio of 0.4 under unaxial tension in direction Z (presented in Fig. 8a) at different stage: (a) fracture pattern at peak load (1626 broken elements); (b) fracure pattern at 1% strain deformation (31588 broken elements); (c) fracture pattern at final stage having an outline out line of anhydrous cement grian (47847 broken elements, the anhydrous cement particle are represented by the blue colour and semi-transparent for clarity).

are nominally identical. Herein, a two-parameter Weibull analysis was used to analyse the 30 simulated strengths in each group with identical w/c ratio. The probability of failure can be written as [61]:

$$\ln\ln\left(\frac{1}{1-P_f}\right) = m\ln\sigma_f - m\ln\sigma_c \quad (4)$$

where P_f is the cumulative probability of failure, m is the Weibull modulus (shape parameter) which is used to describe variability in measured material strength of brittle materials, σ_f is the fracture strength and σ_c is the scaling parameter (characteristic strength). At the characteristic strength, the value of P_f equals 0.63 indicating that 63% of specimens will fail at or below σ_c. In the absence of

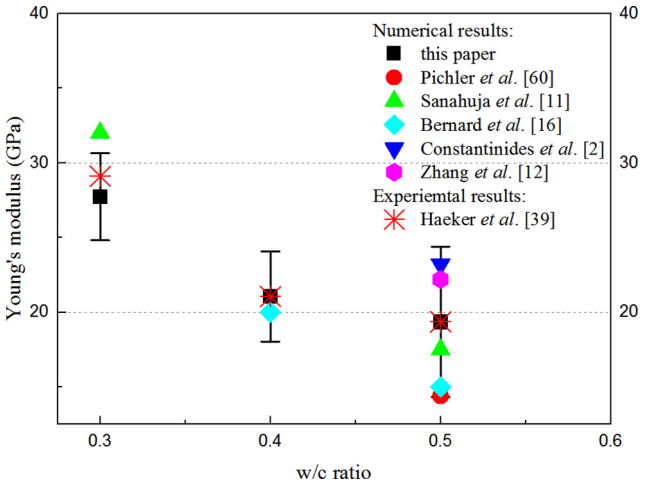

Fig. 11. Comparison of predicted Young's modulus with other micromechanics models together with experimental results.

specific requirements, a general rule-of-thumb is that approximately 30 test specimens provide adequate Weibull strength distribution parameters, with more test specimens contributing little towards better uncertainty estimates [62,63]. Therefore, considering the number of specimens tested in each group, a good regression can be expected if the strength of cement paste at micro scale can be represented by the two-parameter Weibull statics. As shown in Fig. 12, the tensile strengths are plotted in a Weibull coordinate system. A least-squares method was used to fit m and σ_c, where m is the slope of the least-squares fit and σ_c can be calculated from the x-intercept of this fit. Note that if the strength values of the specimens in the group have an infinite scatter, then the fitted line in Fig. 12 would be vertical and the Weibull modulus would approach zero. Conversely, a Weibull modulus approaching infinity would correspond to a group with specimens have exactly the same strength with each other and a horizontal line can be expected in Fig. 12 for this case. The fitted results are given in Table 6. A determination coefficient (R^2) higher than 0.95 is observed for all three groups, which means a strong linear relationship between $\ln\ln(1/1-P_f)$ and $\ln\sigma_f$ exists and indicates that the fracture process is mostly dominated by one type of flaw. From Table 6, it can be seen that, with the increase of w/c ratio, the strength decreases and

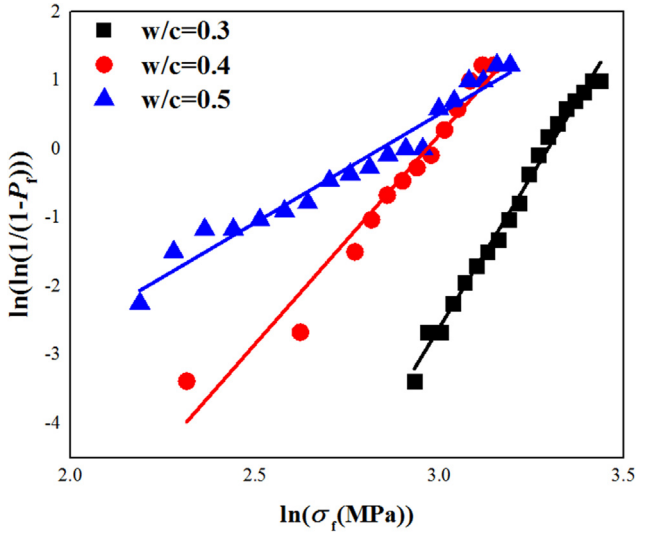

Fig. 12. Weibull plot of for simulated tensile strength of cement paste with different w/c ratios.

Table 6
Weibull parameters for the simulated tensile strength.

w/c ratio	Weibull modulus m	Scaling parameter σ_0	Determination coefficient R^2
0.3	8.85	26.96	0.99
0.4	6.11	19.42	0.98
0.5	3.17	17.10	0.96

becomes more variable. Consequently, both m and σ_c in terms of strengths in each group decrease with w/c ratio increasing. For a better understanding of this issue, the typical fracture pattern of specimens with each w/c ratio is presented in Fig. 13. It is apparent that micro-cracks are less localized in the paste with lower w/c ratio due to the higher amount of anhydrous cement grains and lower porosity in its microstructure, which results in a more stable crack propagation and branching and therefore higher and less varied strength is expected, and more fracture energy is released during the crack propagation. This is opposite to the results from [64] in which the material structure is generated based on modelling. As cement clinkers are assumed as spheres for hydration simulation, different material structures, especially the pore structures are expected [65]. It is important to comment on the nature of the characteristic strength. The characteristic strength is akin to the median strength below which 50% of the fractures would fall. In general, the median and the mean of a distribution are similar but the difference between the median and the mean depends on the details of the distribution. Likewise, the characteristic strength and the mean strength are typically similar but not equal and with respect to this study the characteristic strength is higher than the mean strength.

4.3. Relationship between porosity and simulated mechanical properties

In the matrix, pores act as stress concentration sites and promote failure under loading by introducing micro-cracks. Hence, an increase in pore volume reduces the elastic modulus, fracture energy, and strength of the material [66]. The shapes, sizes and locations of pores are all parameters affecting the deformation and fracture properties [67]. Among these, porosity is regarded as the governing parameter for mechanical properties of porous materials [68]. Although many efforts have been made to correlate mechanical properties with porosity for cement-based materials [69–75], few of them have focused on the micro metre scale. In order to study the micromechanical properties-porosity relation of cement-based materials, the predicted mean strength and Young's modulus of specimens are plotted against their porosity in Fig. 14. It is observed that, regardless of the w/c ratio, these two key mechanical properties decrease continuously with porosity increasing. Therefore, data of cement paste with different w/c ratio are combined for a micromechanical properties-porosity empirical relation study.

With respect to porous materials, quite a few equations have been proposed and developed for expressing the effect of porosity on strength and on Young's modulus in literature [76–81]. For strength, typically four types of relationships in form of linear ($\sigma_P = \sigma_0(1 - kP)$) [76], power exponent ($\sigma_P = \sigma_0\ (1 - P)^k$) [77], exponential ($\sigma_P = \sigma_0 e^{-kP}$) [78] and logarithmic ($\sigma_P = k\ln(P_0/P)$) [79], are most widely used. In all these relationships, σ_P stands for tensile strength at porosity P, σ_0 stands for tensile strength at zero porosity, P_0 stands for porosity at zero strength, k is an empirical constant which can be fit from the experimental results. In analogy to expression for porosity-strength relationships, the Young's modulus-porosity relationship can be expressed as $E_P = E_0(1 - kP)$ [76], ($E_P = E_0\ (1 - P)^k$) [80] and $E_P = E_0 e^{-kP}$ [81]. Analogously, E_P denotes elasticity modulus at porosity P, E_0 is the

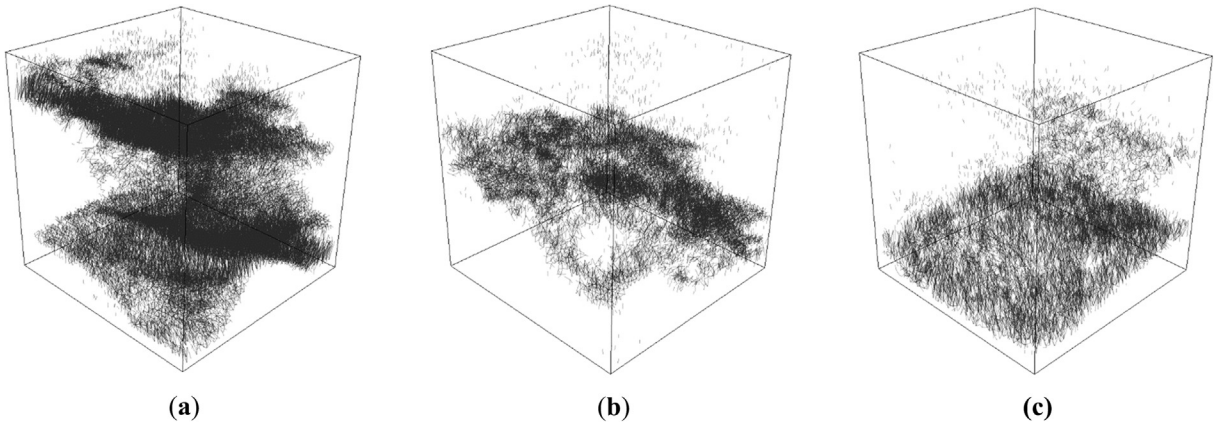

Fig. 13. Typical crack patterns in the final failure state of cement paste with w/c ratio (a) 0.3; (b) 0.4; (c) 0.5.

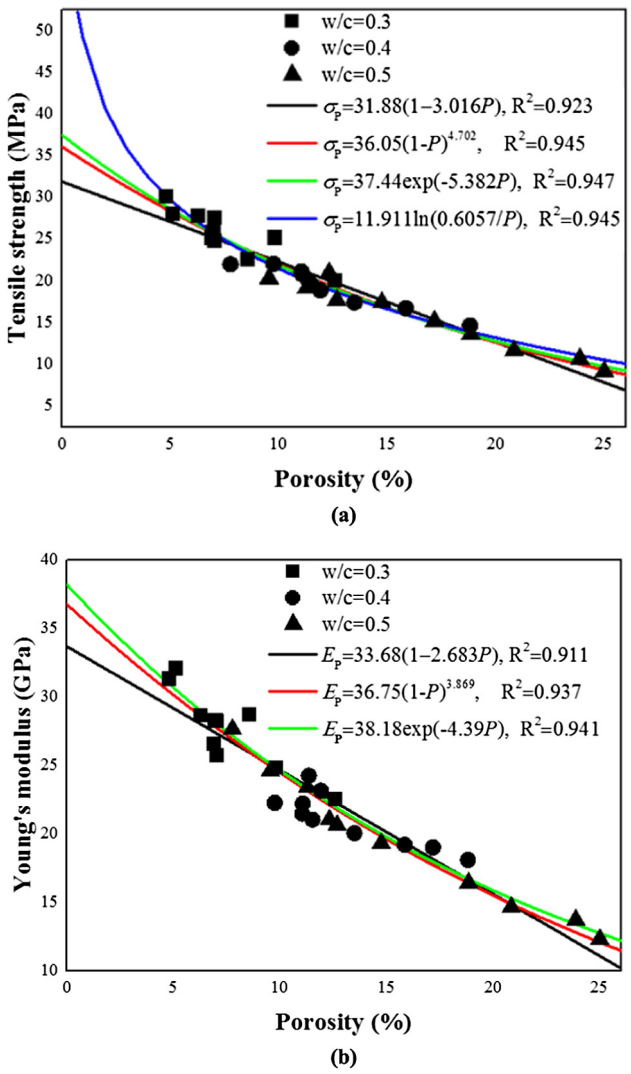

Fig. 14. Relationship between predicted mechanical properties and porosity. (a) strength-porosity relation; (b) elastic modulus-porosity relation.

elasticity modulus at zero porosity. Results of fitting mentioned models of strength–porosity and modulus–porosity relations are given in Fig. 14. All these empirical equations show a good agreement with the simulated results, while exponential curve yields the highest determination coefficient values in both strength–porosity and modulus–porosity fitting (0.947 for strength and 0.941 for modulus). It should be kept in mind that this exponential equation does not satisfy the boundary condition that σ_P or E_P goes to zero as P approaches 1, demonstrating that these empirically developed equations are valid for a limited porosity range. The predicted results in forms of exponential and power are quite close to each other and it is reported in [82] that these results can be made to approximate each other and can be used with satisfactory results. According to these two equations, uniaxial tensile strength of non-porous cement paste is estimated to be around 36 and 37 MPa, while the modulus is around 36 and 38 GPa. Furthermore, it is also important to notice that the k in the power equation for modulus-porosity relation indicates the irregularity degree of a pore structure and it is concluded that, in the polycrystalline materials [83], for closed spherical pores $k = 2$ and for random orientated pores $k = 4$. Therefore, a highly random orientated pore structure is expected for the investigated material structure at micro-scale according to $k = 3.87$ in this study. The Logarithmic model determines a percolation threshold as 60.57% at which porosity the material yields zero strength. However, as shown in Fig. 14a when P approaches 0, an infinite strength is predicted, which is of course not possible. As all empirical models in Fig. 14a and b give good fitting results within the tested porosity range, to determine which model predict more realistic results, it is essential to broaden the modelling results of specimens with porosity lower than 5% and higher than 25%. This can be done by applying the computational uniaxial tension tests on the specimens with lower and higher w/c ratios, respectively.

Furthermore, it should be emphasized that the estimated values of the parameter σ_0, P_0 and E_0 may not always provide a reliable estimate due to the limited resolution of the digitalised material structure and size effect. For example, the sub-micron features in hydrated cement paste [40–42], especially the porosity, cannot be takin into account in the current work. Therefore, the estimated σ_0, P_0 and E_0 involve microstructural details lower than the current resolution, like density of cement grains, hydration products and defects [72,74,75]. Hence, one should be careful with how these fitted parameters are used in practical applications.

4.4. Relation between tensile strength and elasticity modulus

As key mechanical properties of porous materials, the ratio between tensile strength and modulus is of great interest from which the deformation ability of the material can be obtained. As shown in Fig. 15, this ratio is found to be between 800 and 1600 in this study, although a higher value of modulus/strength (10,000) is expected at the concrete scale [33]. Recent micro-cantilever

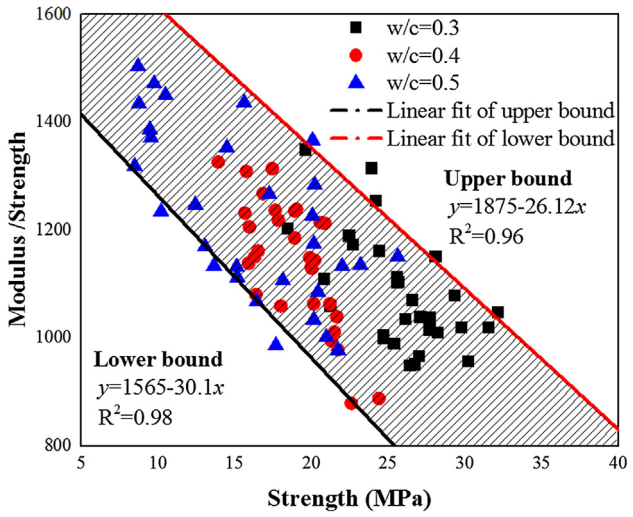

Fig. 15. Relationship between predicted modulus/strength ratio and strength.

measurements of induvial components in hydrated cement paste matrix show even lower values (outer hydration product: around 90, inner hydration products: around 48) [57]. This is because less defects are involved in the material on small length scales [20]. Griffith concluded from measuring glass fibres with small diameter that this ratio can approach 9 when no defect is present in the tested material [84]. Recent measurements of the elastic properties and intrinsic strength of free-standing monolayer graphene membranes reveal that the intrinsic strength can be as even high as $E/8$ [85]. Therefore, the results obtained in this research are regarded reasonable and it can be concluded that the modulus/strength ratio decreases with the investigated length-scale decreasing. This indicates that, with respect to cement paste, smaller specimens will have more strain at the failure stress compared to the larger specimens.

Furthermore, a general trend that the modulus/strength ratio decreases with the increasing of strength (decreasing of porosity) is observed, which means that the strength is more sensitive to defects compared to elastic stiffness. This can be explained by a theory proposed by Hasselam [76] as shown in Fig. 16. While a material is under loading, a stress-free zone exists above and below the defects in the direction of the applied stress. Because neither the pore nor the material in the stress-free zone is stressed, they do not contribute to the strength. Consequently, with increasing porosity, the material of load-bearing area oriented perpendicularly to the applied stress would be reduced not only by the intersected pore but also the additional stress-free zone. Therefore,

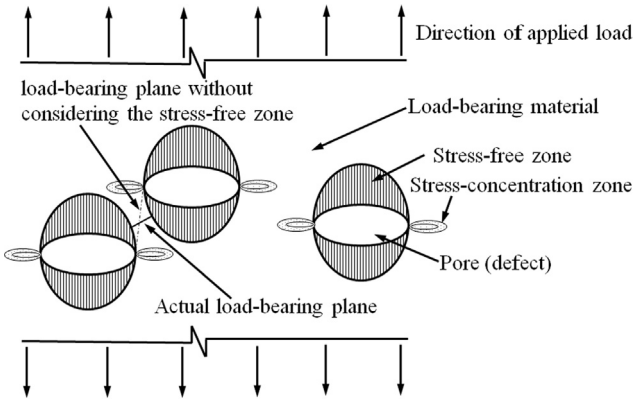

Fig. 16. Schematic view of the model for the effect of porosity on strength.

the effect of porosity on strength is expected to be more significant than on elastic stiffness. As a specimen with lower w/c ratio always has a lower porosity than the one with higher w/c ratio, its modulus/strength ratio is lower. Additionally, two linear bounds were fitted by the data at the edge (Fig. 15). The area within the bonds covers 92.2% results. Note that these bounds are based on data fitting only and should not be confused with analytical bounds existing for elastic modulus (e.g. Hashin-Shtrikhman or Voigt-Reuss).

5. Conclusions

The study level of this paper was chosen to be at micro scale where distinct microscale phases like anhydrous cement grains, capillary pores, inner and outer hydration products can be distinguished. The stochastic micromechanical properties of cement paste were successfully predicted by lattice fracture model using microstructures randomly extracted from XCT images. The following conclusions can be reached from the presented numerical simulations:

The micromechanical properties of cement paste vary a lot due to the heterogeneous nature of its material structure. It is found that most of the predicted modulus at microscale fall into the range of our predicted results, which indicates that the difference between their predicted results can be mainly explained by the heterogeneous nature of this material. Therefore, those who are studying the micromechanical properties of cement paste should be careful with the stochastic nature of such material.

A two-parameter Weibull statistic formula is able to describe the stochastic strength of cement paste prepared with the identical w/c ratio. It is found that Weibull modulus and characteristic strength of specimens decrease with their w/c ratio increasing. This revels that specimens prepared with lower initial w/c ratio have higher and less variable strength value.

Over the examined porosity, ranging from 5% to 25%, all the tested empirical equations can be regarded as good representations for both strength–porosity and modulus–porosity relationships. It is estimated that the micromechanical properties of cement paste can be increased to around 36–37 MPa for strength and 36–38 GPa for Young's modulus, if initial flaws (i.e. pore) larger than 2 μm can be eliminated from the material structure.

The modulus/strength ratio falls in the range between 800 and 1600 at the investigated length scale, which is larger than the one at molecular scale (8–9) but smaller than one at meso scale (around 10000). the predicted results are therefore regarded reasonable and proves that a size effect exists in the modulus/strength ratio.

Conflicts of interest

The authors declare no conflict of interest.

Acknowledgements

This work is supported in part by the scholarship from China Scholarship Council (CSC) under grant CSC No. 201506120067. The authors would also like to acknowledge the help of Mr. Arjan Thijssen with XCT experiments.

References

[1] F.-J. Ulm, G. Constantinides, F. Heukamp, Is concrete a poromechanics materials?—A multiscale investigation of poroelastic properties, Mater. Struct. 37 (2004) 43–58.
[2] G. Constantinides, F.-J. Ulm, The effect of two types of CSH on the elasticity of cement-based materials: results from nanoindentation and micromechanical modeling, Cem. Concr. Res. 34 (2004) 67–80.

[3] G. Constantinides, F.-J. Ulm, K. Van Vliet, On the use of nanoindentation for cementitious materials, Mater. Struct. 36 (2003) 191–196.
[4] C. Hu, Z. Li, A review on the mechanical properties of cement-based materials measured by nanoindentation, Constr. Build. Mater. 90 (2015) 80–90.
[5] K. Velez, S. Maximilien, D. Damidot, G. Fantozzi, F. Sorrentino, Determination by nanoindentation of elastic modulus and hardness of pure constituents of Portland cement clinker, Cem. Concr. Res. 31 (2001) 555–561.
[6] P.D. Tennis, H.M. Jennings, A model for two types of calcium silicate hydrate in the microstructure of Portland cement pastes, Cem. Concr. Res. 30 (2000) 855–863.
[7] P. Trtik, J. Kaufmann, U. Volz, On the use of peak-force tapping atomic force microscopy for quantification of the local elastic modulus in hardened cement paste, Cem. Concr. Res. 42 (2012) 215–221.
[8] M. Luković, E. Schlangen, G. Ye, Combined experimental and numerical study of fracture behaviour of cement paste at the microlevel, Cem. Concr. Res. 73 (2015) 123–135.
[9] C. Hu, Z. Li, Micromechanical investigation of Portland cement paste, Constr. Build. Mater. 71 (2014) 44–52.
[10] M. Zhang, A.P. Jivkov, Microstructure-informed modelling of damage evolution in cement paste, Constr. Build. Mater. 66 (2014) 731–742.
[11] J. Sanahuja, L. Dormieux, G. Chanvillard, Modelling elasticity of a hydrating cement paste, Cem. Concr. Res. 37 (2007) 1427–1439.
[12] M. Zhang, A.P. Jivkov, Micromechanical modelling of deformation and fracture of hydrating cement paste using X-ray computed tomography characterisation, Compos. B Eng. 88 (2016) 64–72.
[13] H. Zhang, B. Šavija, S. Chaves Figueiredo, M. Lukovic, E. Schlangen, Microscale Testing and Modelling of Cement Paste as Basis for Multi-Scale Modelling, Materials 9 (2016) 907.
[14] M. Hlobil, V. Šmilauer, G. Chanvillard, Micromechanical multiscale fracture model for compressive strength of blended cement pastes, Cem. Concr. Res. 83 (2016) 188–202.
[15] Z. Qian, E. Schlangen, G. Ye, K. van Breugel, Modeling Framework for Fracture in Multiscale Cement-Based Material Structures, Materials 10 (2017) 587.
[16] O. Bernard, F.-J. Ulm, E. Lemarchand, A multiscale micromechanics-hydration model for the early-age elastic properties of cement-based materials, Cem. Concr. Res. 33 (2003) 1293–1309.
[17] B. Šavija, H. Zhang, E. Schlangen, Influence of Microencapsulated Phase Change Material (PCM) Addition on (Micro) Mechanical Properties of Cement Paste, Materials 10 (2017) 863.
[18] H. Zhang, B. Šavija, E. Schlangen, Combined experimental and numerical study on micro-cube indentation splitting test of cement paste, Eng. Fract. Mech. (2018), https://doi.org/10.1016/j.engfracmech.2018.04.018.
[19] F. Bernard, S. Kamali-Bernard, W. Prince, 3D multi-scale modelling of mechanical behaviour of sound and leached mortar, Cem. Concr. Res. 38 (2008) 449–458.
[20] H. Zhang, B. Šavija, S.C. Figueiredo, E. Schlangen, Experimentally validated multi-scale modelling scheme of deformation and fracture of cement paste, Cem. Concr. Res. 102 (2017) 175–186.
[21] K. Van Breugel, Numerical simulation of hydration and microstructural development in hardening cement-based materials:(II) applications, Cem. Concr. Res. 25 (1995) 522–530.
[22] S. Bishnoi, K.L. Scrivener, μic: a new platform for modelling the hydration of cements, Cem. Concr. Res. 39 (2009) 266–274.
[23] J.W. Bullard, E.J. Garboczi, A model investigation of the influence of particle shape on portland cement hydration, Cem. Concr. Res. 36 (2006) 1007–1015.
[24] B. Pichler, C. Hellmich, J. Eberhardsteiner, Spherical and acicular representation of hydrates in a micromechanical model for cement paste: prediction of early-age elasticity and strength, AcMec 203 (2009) 137–162.
[25] D.P. Bentz, D.P. Bentz, CEMHYD3D: A Three-Dimensional Cement Hydration and Microstructure Development Modelling Package. Version 2.0, US Department of Commerce, National Institute of Standards and Technology, 2000.
[26] M. Hain, P. Wriggers, Numerical homogenization of hardened cement paste, CompM 42 (2008) 197–212.
[27] T. Chotard, M. Boncoeur-Martel, A. Smith, J. Dupuy, C. Gault, Application of X-ray computed tomography to characterise the early hydration of calcium aluminate cement, Cem. Concr. Compos. 25 (2003) 145–152.
[28] M.A.B. Promentilla, T. Sugiyama, T. Hitomi, N. Takeda, Quantification of tortuosity in hardened cement pastes using synchrotron-based X-ray computed microtomography, Cem. Concr. Res. 39 (2009) 548–557.
[29] M. Zhang, Y. He, G. Ye, D.A. Lange, K. van Breugel, Computational investigation on mass diffusivity in Portland cement paste based on X-ray computed microtomography (μCT) image, Constr. Build. Mater. 27 (2012) 472–481.
[30] G.T. Herman, Fundamentals of Computerized Tomography: Image Reconstruction from Projections, Springer Science & Business Media, 2009.
[31] J.J. Chen, L. Sorelli, M. Vandamme, F.J. Ulm, G. Chanvillard, A Coupled nanoindentation/SEM-EDS study on low water/cement ratio portland cement paste: evidence for C-S–H/Ca(OH)2 nanocomposites, J. Am. Ceram. Soc. 93 (2010) 1484–1493.
[32] E. Schlangen, E. Koenders, K. Van Breugel, Influence of internal dilation on the fracture behaviour of multi-phase materials, Eng. Fract. Mech. 74 (2007) 18–33.
[33] E. Schlangen, E. Garboczi, Fracture simulations of concrete using lattice models: computational aspects, Eng. Fract. Mech. 57 (1997) 319–332.
[34] M. Nikolić, E. Karavelić, A. Ibrahimbegovic, P. Miščević, Lattice Element Models and Their Peculiarities, Arch. Comput. Methods Eng. (2017) 1–32.
[35] M. Luković, B. Šavija, E. Schlangen, G. Ye, K. van Breugel, A 3D lattice modelling study of drying shrinkage damage in concrete repair systems, Materials 9 (2016) 575.
[36] H. Wong, M. Head, N. Buenfeld, Pore segmentation of cement-based materials from backscattered electron images, Cem. Concr. Res. 36 (2006) 1083–1090.
[37] K.L. Scrivener, Backscattered electron imaging of cementitious microstructures: understanding and quantification, Cem. Concr. Compos. 26 (2004) 935–945.
[38] K. Van Breugel, Simulation of Hydration and Formation of Structure in Hardening Cement-based Materials, Delft University of Technology, Delft, The Netherlands, 1991.
[39] C.-J. Haecker, E. Garboczi, J. Bullard, R. Bohn, Z. Sun, S. Shah, T. Voigt, Modeling the linear elastic properties of Portland cement paste, Cem. Concr. Res. 35 (2005) 1948–1960.
[40] H. Ma, Z. Li, Realistic pore structure of Portland cement paste: experimental study and numerical simulation, Comput. Concr 11 (2013) 317–336.
[41] H. Ma, D. Hou, Y. Lu, Z. Li, Two-scale modeling of the capillary network in hydrated cement paste, Constr. Build. Mater. 64 (2014) 11–21.
[42] H. Ma, D. Hou, Z. Li, Two-scale modeling of transport properties of cement paste: Formation factor, electrical conductivity and chloride diffusivity, Comput. Mater. Sci. 110 (2015) 270–280.
[43] T.C. Powers, T.L. Brownyard, Studies of the physical properties of hardened Portland cement paste, Journal Proceedings (1946) 101–132.
[44] R.A. Cook, K.C. Hover, Mercury porosimetry of hardened cement pastes, Cem. Concr. Res. 29 (1999) 933–943.
[45] Z. Pan, R. Ma, D. Wang, A. Chen, A review of lattice type model in fracture mechanics: theory, applications, and perspectives, Eng. Fract. Mech. 190 (2018) 382–409.
[46] E. Schlangen, Z. Qian, 3D modeling of fracture in cement-based materials, J. Multiscale Modell. 1 (2009) 245–261.
[47] G. Lilliu, J.G. van Mier, 3D lattice type fracture model for concrete, Eng. Fract. Mech. 70 (2003) 927–941.
[48] G. Lilliu, 3D analysis of Fracture Processes in Concrete, Delft University of Technology, Delft, The Netherlands, 2007.
[49] E. Schlangen, Experimental and Numerical Analysis of Fracture Processes in Concrete Ph.D. Thesis, Delft University of Technology, Delft, The Netherlands, 1993.
[50] A. Delaplace, G. Pijaudier-Cabot, S. Roux, Progressive damage in discrete models and consequences on continuum modelling, J. Mech. Phys. Solids 44 (1996) 99–136.
[51] H.J. Herrmann, A. Hansen, S. Roux, Fracture of disordered, elastic lattices in two dimensions, PhRvB 39 (1989) 637.
[52] M. Yip, J. Mohle, J. Bolander, Automated Modeling of Three-Dimensional Structural Components Using Irregular Lattices, Comput.-Aided Civ. Infrastruct. Eng. 20 (2005) 393–407.
[53] Z. Qian, E. Schlangen, G. Ye, K. Van Breugel, Prediction of mechanical properties of cement paste at microscale, Materiales de Construccion 60 (2010) 7–18.
[54] I. Odler, M. Rößler, Investigations on the relationship between porosity, structure and strength of hydrated Portland cement pastes. II. Effect of pore structure and of degree of hydration, Cem. Concr. Res. 15 (1985) 401–410.
[55] D. Liu, K. Mingard, O.T. Lord, P. Flewitt, On the damage and fracture of nuclear graphite at multiple length-scales, JNuM 493 (2017) 246–254.
[56] B. Šavija, D. Liu, G. Smith, K.R. Hallam, E. Schlangen, P.E. Flewitt, Experimentally informed multi-scale modelling of mechanical properties of quasi-brittle nuclear graphite, Eng. Fract. Mech. 153 (2016) 360–377.
[57] J. Němeček, V. Králík, V. Šmilauer, L. Polívka, A. Jäger, Tensile strength of hydrated cement paste phases assessed by micro-bending tests and nanoindentation, Cem. Concr. Compos. 73 (2016) 164–173.
[58] E. Schlangen, Crack development in concrete, Part 1: Fracture experiments and CT-scan observations, Trans. Tech. Publ. Key Eng. Mater. (2008) 69–72.
[59] E. Schlangen, Crack development in concrete, part 2: modelling of fracture process, Trans. Tech. Publ. Key Eng. Mater. (2008) 73–76.
[60] B. Pichler, C. Hellmich, Upscaling quasi-brittle strength of cement paste and mortar: A multi-scale engineering mechanics model, Cem. Concr. Res. 41 (2011) 467–476.
[61] J.B. Wachtman, W.R. Cannon, M.J. Matthewson, Mechanical Properties of Ceramics, John Wiley & Sons, 2009.
[62] J.B. Quinn, G.D. Quinn, A practical and systematic review of Weibull statistics for reporting strengths of dental materials, Dent. Mater. 26 (2010) 135–147.
[63] D.R. Thoman, L.J. Bain, C.E. Antle, Inferences on the parameters of the Weibull distribution, Technometrics 11 (1969) 445–460.
[64] Z. Qian, Multiscale Modeling of Fracture Processes in Cementitious Materials, Delft University of Technology, Delft, The Netherlands, 2012.
[65] H. Dong, P. Gao, G. Ye, Characterization and comparison of capillary pore structures of digital cement pastes, Mater. Struct. 50 (2017) 154.
[66] D. Liu, B. Šavija, G.E. Smith, P.E. Flewitt, T. Lowe, E. Schlangen, Towards understanding the influence of porosity on mechanical and fracture behaviour of quasi-brittle materials: experiments and modelling, Int. J. Fract. (2017) 1–16.
[67] H. Chandler, I. Merchant, R. Henderson, D. Macphee, Enhanced crack-bridging by unbonded inclusions in a brittle matrix, J. Eur. Ceram. Soc. 22 (2002) 129–134.
[68] M.Y. Corapcioglu, Advances in Porous Media, Elsevier, 1996.
[69] C. Lian, Y. Zhuge, S. Beecham, The relationship between porosity and strength for porous concrete, Constr. Build. Mater. 25 (2011) 4294–4298.

[70] X. Chen, S. Wu, J. Zhou, Influence of porosity on compressive and tensile strength of cement mortar, Constr. Build. Mater. 40 (2013) 869–874.
[71] R. Kumar, B. Bhattacharjee, Porosity, pore size distribution and in situ strength of concrete, Cem. Concr. Res. 33 (2003) 155–164.
[72] D.M. Roy, G.R. Gouda, Porosity-strength relation in cementitious materials with very high strengths, J. Am. Ceram. Soc. 56 (1973) 549–550.
[73] M. Röβler, I. Odler, Investigations on the relationship between porosity, structure and strength of hydrated portland cement pastes I. Effect of porosity, Cem. Concr. Res. 15 (1985) 320–330.
[74] Y.-X. Li, Y.-M. Chen, J.-X. Wei, X.-Y. He, H.-T. Zhang, W.-S. Zhang, A study on the relationship between porosity of the cement paste with mineral additives and compressive strength of mortar based on this paste, Cem. Concr. Res. 36 (2006) 1740–1743.
[75] M. Relis, I. Soroka, Compressive strength of low-porosity hydrated portland cement, J. Am. Ceram. Soc. 63 (1980) 690–694.
[76] D. Hasselman, Relation between effects of porosity on strength and on Young's modulus of elasticity of polycrystalline materials, J. Am. Ceram. Soc. 46 (1963) 564–565.
[77] M.Y. Balshin, Relation of mechanical properties of powder metals and their porosity and the ultimate properties of porous metal-ceramic materials, Dokl Akad Nauk SSSR (1949) 831–834.
[78] W. Duckworth, Discussion of Ryshkewitch paper, J. Am. Ceram. Soc. 36 (1953) 68.
[79] K. Schiller, Strength of porous materials, Cem. Concr. Res. 1 (1971) 419–422.
[80] G. McAdam, Some relations of powder characteristics to the elastic modulus and shrinkage of sintered ferrous compacts, Journal of the Iron and Steel institute 168 (1951) 346.
[81] R. Spriggs, Expression for effect of porosity on elastic modulus of polycrystalline refractory materials, particularly aluminum oxide, J. Am. Ceram. Soc. 44 (1961) 628–629.
[82] F. Knudsen, Dependence of mechanical strength of brittle polycrystalline specimens on porosity and grain size, J. Am. Ceram. Soc. 42 (1959) 376–387.
[83] A. Maitra, K.K. Phani, Ultrasonic evaluation of elastic parameters of sintered powder compacts, Journal of materials science 29 (1994) 4415–4419.
[84] A.A. Griffith, The phenomena of rupture and flow in solids, Philosophical transactions of the royal society of london, Series A, containing papers of a mathematical or physical character 221 (1921) 163–198.
[85] C. Lee, X. Wei, J.W. Kysar, J. Hone, Measurement of the elastic properties and intrinsic strength of monolayer graphene, Science 321 (2008) 385–388.